

Review Article

Evaluation of Prestrain Annealing Impact on Nanomaterial Sensitization

T. N. Suresh Kumar,¹ T. Deepa ,² L. Natrayan ,³ Marabathina Maheedhar,² and Raja Kathiravan ⁴

¹Department of Mechanical Engineering, Dhaanish Ahmed College of Engineering, Chennai, 601301 Tamil Nadu, India

²School of Electrical Engineering, VIT University, Chennai, 600 127 Tamil Nadu, India

³Department of Mechanical Engineering, Saveetha School of Engineering, SIMATS, Chennai, 602105 Tamil Nadu, India

⁴Department of Mechanical Engineering, Bahir Dar Institute of Technology, Bahir Dar University, Bahir Dar 6000, Ethiopia

Correspondence should be addressed to T. Deepa; deepa.t@vit.ac.in, L. Natrayan; natrayanphd@gmail.com, and Raja Kathiravan; kathirrk3000@gmail.com

Received 25 July 2021; Revised 10 September 2021; Accepted 18 September 2021; Published 5 October 2021

Academic Editor: Lakshmipathy R

Copyright © 2021 T. N. Suresh Kumar et al. This is an open access article distributed under the Creative Commons Attribution License, which permits unrestricted use, distribution, and reproduction in any medium, provided the original work is properly cited.

Light metal alloys are extensively used in automotive, aerospace, aircraft, and military sectors since their lightweight leads to reduced energy consumption, increased fuel efficiency, and better environmental protection. In the present situation, nanomaterials are the potential candidate for weight saving in the structural application and can meet stringent government norms. Nanomaterial was heat-treated in the furnace to about a certain temperature and time and then normalized for strengthening. The heat-treated nanomaterial undergoes different forging processes, namely, hot forging and cold forging, using a certain capacity's hydraulic press. Hence, in this work, an extensive study on the influence of the prestrain annealing, the corrosion rate on differently treated samples, and the effect of sensitization heat treatment on the nanomaterial was done.

1. Introduction

Until cooling, the nanomaterial must be heated above its recrystallization temperature for a specified period. The cooling rate is determined by the metals being annealed [1]. Steel is typically permitted to cool to room temperature in still air, whereas copper, silver, and brass can be cooled slowly in the air or quenched quickly in water [2]. The heating process causes atoms in the crystal lattice to migrate, reducing the number of dislocations and altering the nanomaterial's ductility and hardness [3]; when the heat-treated nanomaterial cools, it recrystallizes. The crystal grain size and phase composition determined by the heating and cooling rates dictate the nanomaterial properties [4]. The silicon as the major alloy element in aluminum alloy improves the strength of the matrix. The Cu and Mg elements are secondary alloying elements in the aluminum matrix, Mg

improves the uniform dispersion of the matrix elements, and Cu improves the matrix strength with a combination of Fe elements. Fe, Ni, Ti, Zn, and Cr are commonly used as minor addition in the aluminum matrix, and their composition varies dependent upon the applications. [5]. In the hot or cold working annealing process, the metal parts change the nanomaterial structure again so additional heat treatments can be needed to achieve the desired properties [6]. The key benefits of annealing are how it increases a nanomaterial's workability by improving durability, decreasing stiffness, and increasing machinability. Metal brittleness is reduced while their magnetic properties and electrical conductivity are improved by the heating and cooling process [7]. Feng et al. have prepared W-TaC alloys by hot pressing and high energy rate forging. For locating thermal surprise resistance of the as-solid samples, ELMS-like thermal surprise had been carried out [8]. The cracking formation of the developed

W-Tac was blocked due to the base temperature that increased to 100°C [9]. The W-Tac alloy density and hardness before and after HERF are shown in Table 1.

Lin et al. reported that galling happens at the die surface's boundary bottom point, in the center of the straight and corner edge. On the other hand, galling begins at the same boundaries' top as the die surface and spreads downward on the drawn cup as drawing cycles progress [10]. On both die and drawn cup surfaces, galling occurs clearly; the SLD nanomaterial shows good performance than SKD11 and ADI [11]. Figure 1 shows that the temperature was extremely high around the boundary between the straight and corner edges.

Sharma et al. focused on laser beam in-field vacuum oven annealing which is compared with CW-laser annealing. There was no loss of texture or surface roughness in this process for laser intensities. The laser annealing process is dependent on heat propagation through the thin-film system and into the substrate; significant changes were observed when the laser processed region was changed [12]. The ceramic particle size, distribution, quantity of reinforcement, and shape of the reinforcement are enhancing the mechanical, tribological, and corrosion properties of the metal matrix composites and also depend on the induced load which is transferred to the reinforcing phase [13]. Kim et al. [14] presented that after low-temperature annealing, it causes diminished leakage current. The thin Te layer is generated during the electroless deposition process, oxidized to TeO₂ or CdTeO₃ at low-temperature annealing. Effective resistance was increased when CZT connected with the thin oxidized layer in series. So, the leakage current is reduced. Zhao et al. investigated LDX 2404 DSS's corrosion behaviour which was presented at 700°C for various aging times. The sigma granular particles phase grows larger but less with aging time. The aged specimen's Ir/Ia current ratios increase with time, but when aging time is more than 16 hr, the change rates become alleviative [15]. As the holding time is extended to 48 hr, corrosion becomes more important, and corrosion form changes to general corrosion [16]. Eggleston et al. presented in this paper which generates higher V_{oc} voltage than the natural belt-furnace annealing process. The silicon or glass interface device attains a steady state at any point. During the process sequence, the substrate temperature reduces from 960°C to 620°C and a max sun voltage of 492 mV is generated. By the reduced processing temperature, cheaper substrates can be used, which reduces the manufacturing cost [17]. He et al. used high mechanical properties in aerospace, automobile, and shipbuilding forging production. This study concentrated on the conversion and consumption of thermal energy in heating and forging. The relationship between nanomaterial flow and energy flow is proportional, according to the study. To reduce heat loss, enterprises have to reduce heat loss and energy-carrying water emission and design a good heating furnace [18].

1.1. Variation of Metal Characteristics under Heat. Maysa Terada et al. [19], reported that the effect of known DIN 14970 steel precipitation conduct on intergranular erosion opposition was examined. M₂₃C₆ residues were found at

TABLE 1: W-Tac alloys' density and hardness before and after HERF [8].

	Density (g/cm ³)	Relative density	Hardness (HV)
AS-sintered	18.646	96.7%	395
AS-forged	19.091	99.05%	533

the boundaries of the solution. By using X-ray diffraction, carbides were found, by the TTP curves; OM, SEM-EDS, and TEM were also listed. Temperatures between 873 and 1073 K display a low sensitivity to intergranular attack in aged specimens [20]. Kosec et al. find the austenite heat-resistant stainless steel transformation kinetics which were discussed. Long-annealed steel samples showed a heavy coarsening of precipitates, as well as a significant amount of phase particles in the form of a chain and network of plates [21]. The hardness of annealing at a temperature of 600°C started to increase after 48 hours, and the hardness increased in the temperature range of 700-900°C. The results concluded that after isothermal annealing, the microstructure steel consisted of austenite, carbide, and σ -phase [22]. Sahlaoui et al. discussed the phenomenological and analytical analysis which was carried out for the depleted chromium zone in Ni-Cr-Fe alloys caused by carbide precipitation during aging to predict the evolution of the chromium profile. Dechromization and rechromization are the two steps in the chromium concentration extraction process. For Inconel 690 heat-treated for various periods and temperatures, the proposed model constants were established. By using an approximate solution, an analytical calculation can correctly describe the dichotomization and rechromization [23]. Lv et al. investigated that at 600 degrees Celsius, the impact of refinement on latent movies outside of 2205 duplex tempered steel was considered. Passive film on the sensitized sample had less corrosion resistance than the solid solution at 0.6 V_{SCE} [24].

The doping focus in the sharpened example is higher than that in the strong arrangement tempered example, resulting in the former's poorer corrosion resistance in the borate buffer solution [25]. Zhang et al. specially considered the impact of isothermal maturing on the consumption conduct of UNS S82441 duplex hardened steel at different occasions utilizing both potentiodynamic polarization and potential static basic pitting temperature strategies. Utilizing morphological perception and electrochemical location, the microstructure advancement and pitting erosion conduct of UNS S82441 DSS matured at 700°C for different occasions were examined. By increasing, aging time corrosion resistance of the specimen decreased [26]. Polarization behaviour and localized corrosion morphology are strongly affected by artificial aging. Zhang and Frankel investigated various AA2024 pitting and intergranular corrosion behaviours in 1 M NaCl. In the arrangement of heat-treated and water extinguished states, the anodic polarization bends of AA2024 T3 and T3+ tempers uncovered two breakdown possibilities. At 190°C breakdown, the potential decreases with an increase in aging [27]. Gorhe et al. investigated alloy 22 as Ni-Cr-Mo-W alloy made for nuclear waste containers'

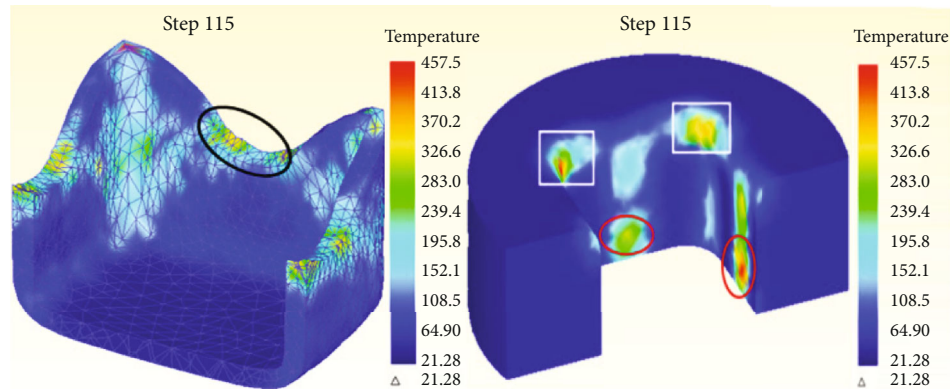


FIGURE 1: Workpiece and die temperature distribution at step 115 [10].

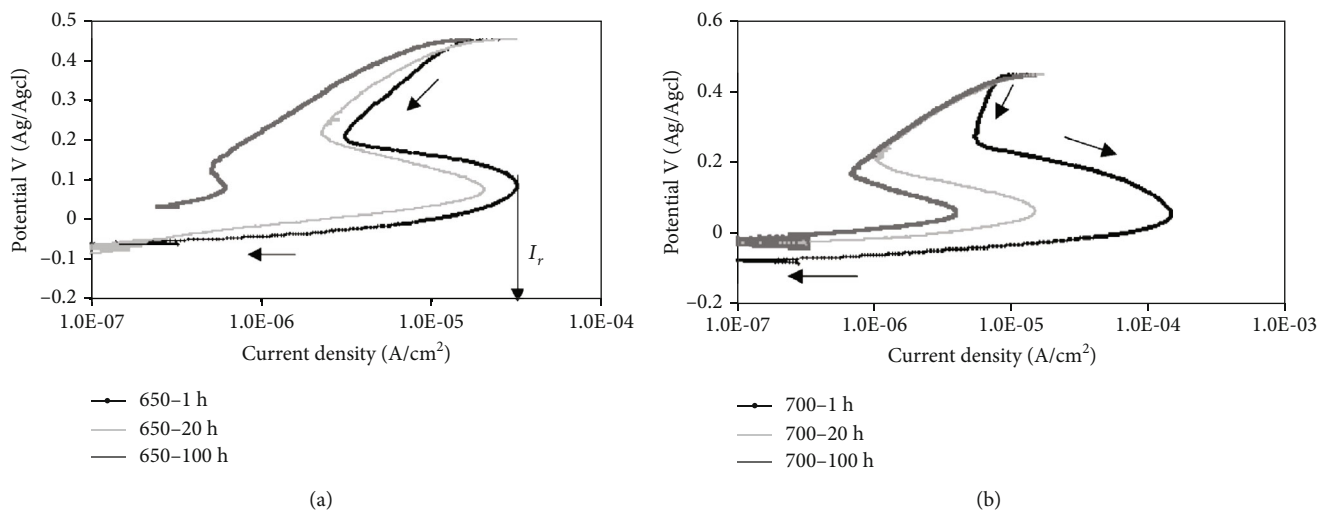


FIGURE 2: (a, b) SL-EPR test for alloy 22 aged at 650°C [28].

outer walls. This study used a variety of electrochemical experiments to confirm the microstructural changes caused by aging and welding. The EPR testing detected that the Cr depletion in 1 M H_2SO_4 +0.5 M NaCl +0.01 M KSCN solution at 30°C for long-duration aging above 650°C replenishes the Cr depletion as reactivation of current peaks decreased [28]. The increase of aging time and reactivation peak current decrease is shown in Figure 2(a). Figure 2(b) shows the same results that are shown in Figure 2(a).

Takahashi et al. reported electromagnetic hoop stress numerical results, σ_{θ}^{FCM} during FCM from 20 T at 50 K, and thermal hoop stress, σ_{θ}^{cool} under cooling, in REBaCuO discs and ring bulks reinforced by SUS ring with various widths, were compared. The maximum of σ_{θ}^{total} at step 6 during FCM was reduced from +216 MPa without SUS ring reinforcement to -29 MPa for $W_{sus}=20$ mm, which is less than that if the disc bulb was used [29]. The wider SUS ring alleviated the tension concentration in the ring bulk, according to the numerical findings [30]. L. Dal Negro et al. [31] reactive RF magnetron sputtering and thermal annealing make Er:SRO samples. Optimizing a temperature range of 600-800°C for annealing temperatures, Er light emission

was demonstrated. With full CMOS compatibility, these Er:SRO films can be used to fabricate compact waveguide optical amplifiers and integrated light sources [32].

1.2. Variation of Metal Characteristics under Different Surrounding and Working Conditions. Chen et al. reported that solvent vapour annealing (SVA) two-step method and thermal annealing (TA) can improve overall system performance, particularly by avoiding reduction in V_{oc} . The use of solvent vapour annealing can improve inefficiency. Unit performance parameters with different annealing treatments under 100 MW/cm² are shown in Table 2. Reduction of V_{oc} can be eliminated when the devices are treated with consequent TA [33].

Ma et al. reported that TMS-PCs of N80 and J55 oil tube steels show a substantial reduction in both uniform and pitting corrosion rates. Since TMS-PCs are hydrophobic, brine solution has a hard time contacting the steel matrix. The corrosion resistance of vacuum direct current plasma coatings (VDCPC) is more excellent than atmospheric direct current plasma coatings (ADCPC). In a brine solution, plasma chemical vapour deposition PCVD

TABLE 2: Unit performance parameters with different annealing treatments under 100 MW/cm^2 [33].

Treatment	V_{oc} (V)	J_{sc} (mA/cm^2)	FF (%)	PCE (%)
None	0.790	8.610	34.30	2.310
SVA	0.7691	14.81	65.41	7.481
SVA+Ta	0.801	15.20	67.70	8.220

TABLE 3: Computational performance comparison [37].

Control type	CPU time at case 1 (s)	CPU time at case 2 (s)
NN	214.50	117.161
Incremental LS-SVM	139.511	0.4830
ELM-based bootstrap	237.361	4.7180
Proposed method	2.44920	0.18721

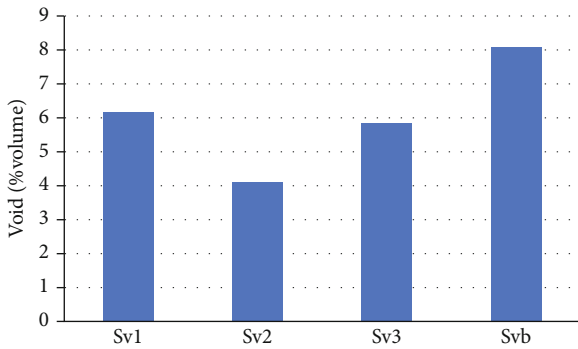


FIGURE 3: Void volume average values in every variation [39].

is a great way to improve tube steel corrosion and pitting resistance [34].

Bahrami and Taheri introduced the IGC of undeformed specimens increasing sensitization temperature and exposure time. A high deformation and low deformation reduce IGC and tend to increase IGC, respectively. On sensitizing condition, transition point concerning deformation is relevant. Grain boundaries were attacked at low levels of deformation, and uniform corrosion can be overcome at high deformation levels. Throughout the matrix, chromium depletion occurs concerning lower local depletion [35]. Chen et al. reported that Ag alloy bonding wires doped with Pd and Au components were produced to replace traditional Au wire. By electrochemical polarization Ag alloy, the wire's corrosion behaviour is tested. Cu wire can be protected by a Pd film from corrosion. Under the potentiodynamic test, Au wire can be completely protected from corrosion [36]. Lu et al. proposed modeling complex batch forging process online probabilistic ELM. Based on the findings, it was determined that probabilistic ELM could accurately represent the distribution behaviour of the batch forging process [37]. Data collected from the new forging distribution model is updated effectively by the developed model update strategy. Table 3 refers to the computation performance [38].

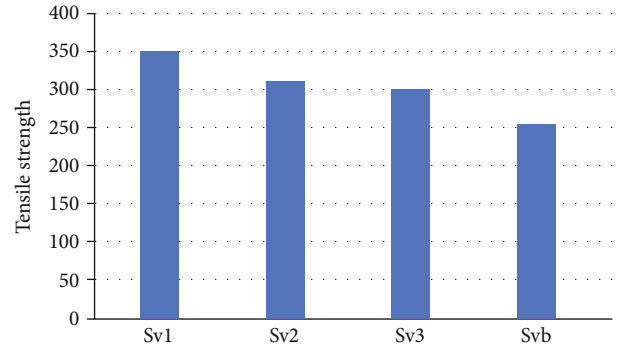


FIGURE 4: Average maximum of tensile stress at each variation [39].

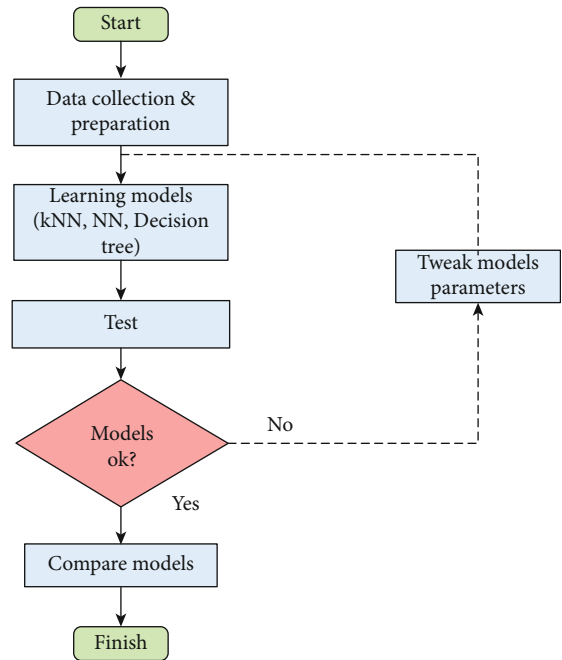


FIGURE 5: Methodology flow chart [42].

In Salman et al.'s study, using the VARI method, maximum tensile stress values were found, but the bending value is not smaller than the hand lay-up method. Figures 3 and 4 show that the smallest void volume average fraction was obtained at the second variety with a 4.2841% void volume average value. The highest void volume fraction was obtained at 8.141% and the highest tensile stress at every variation [39].

Li et al. investigated the effect of grain size on 316L SS intergranular corrosion. Both DLEPR tests and microstructure inspection indicate that 316L SS becomes less susceptible to intergranular corrosion as grain size increases. At long-duration high temperatures, the intergranular corrosion resistance of 316L is improved [40]. The current study indicates that raising the grain size to an optimal level effectively increases the intergranular corrosion resistance of 316L stainless steel [41]. Alhindawi and Altarazi reported that predicting the tensile strength of extrusion-blown HDPE film has been demonstrated by applying CART, KNN, and ANN. This algorithm can achieve the required

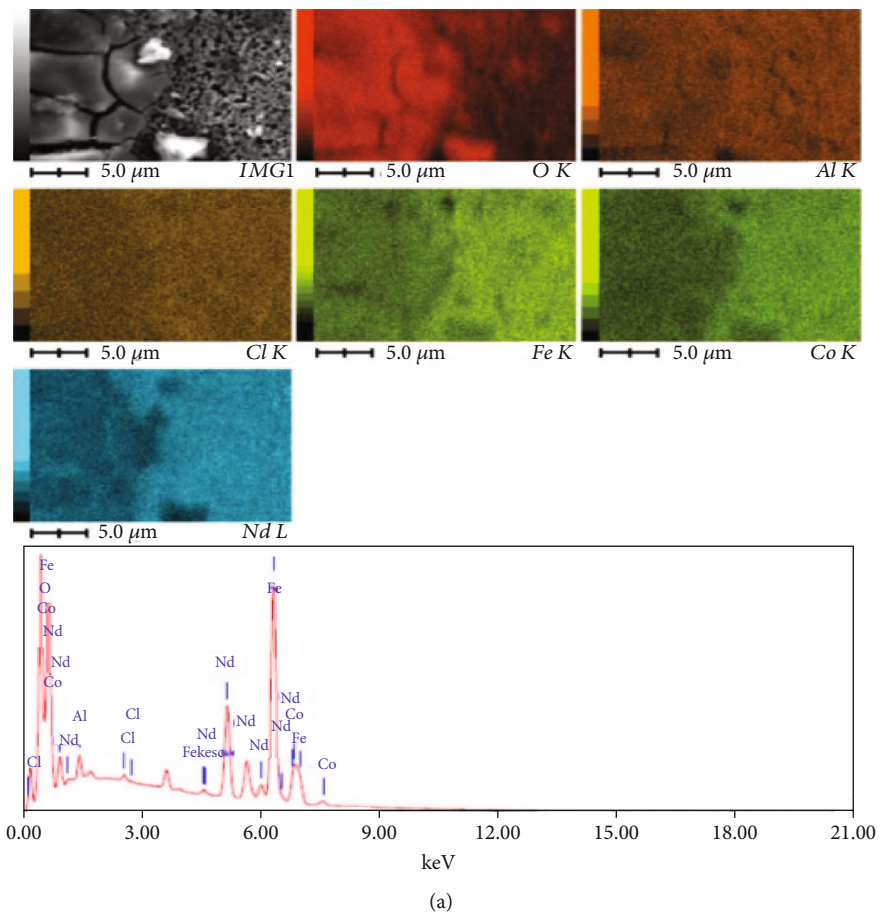


FIGURE 6: Continued.

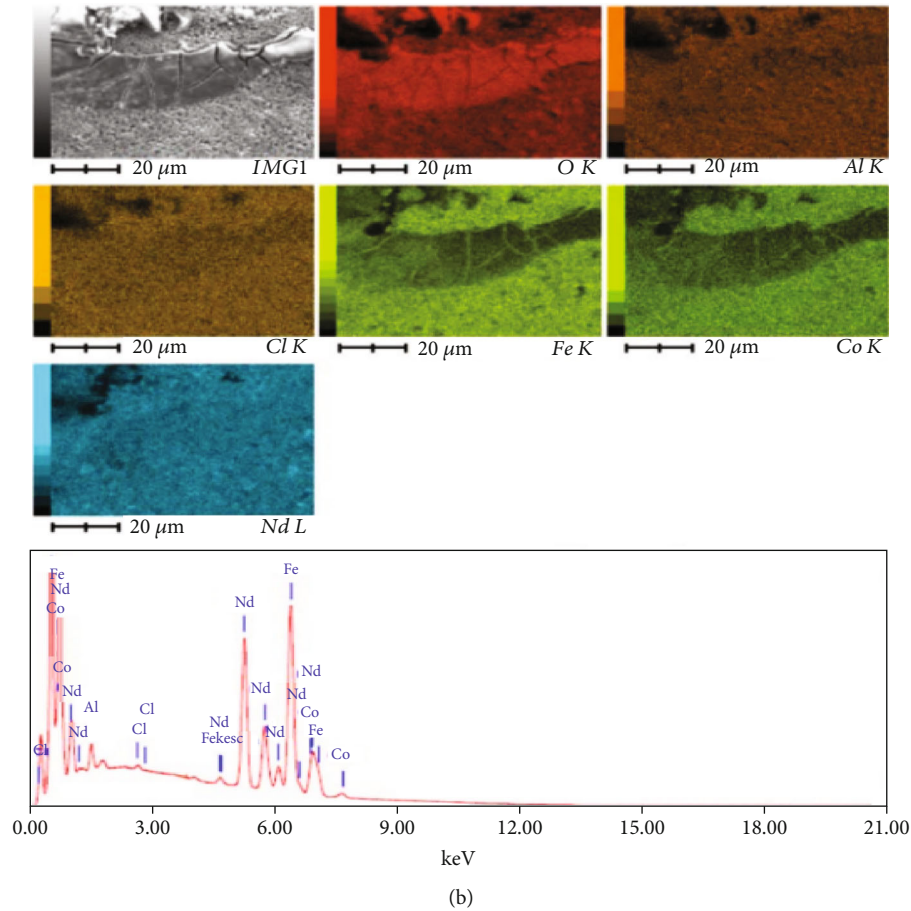


FIGURE 6: EDS and elemental mapping of corroded samples from a defined area: (a) ND15Al3 composition; (b) ND20Al3 composition [43].

tensile strength. Figure 5 shows the methodology flow-chart [42].

Parmar et al. reported that alloy composition was made by microwave combustion, followed by a reduction diffusion process. Nd₂(FeCo)₁₄B hard magnet corrosion resistance increased by adding Al by 3% and again increased by replacing Fe by 5% Nd. 5% substitution of Nd improved both coercivity and corrosion resistance. The majority phase protects from corrosion but the minority phase dissolves. By Ni plating, both the Al and Nd substituted sample corrosion resistance improved. The Nd substitute's best potential corrosion values and current density appear by 10 μm thickness of Ni plating. SEM-EDS analyzed ND15Al3 and ND20Al3 corroded portions [43]. Figure 6(a) shows the oxide elements in the corroded part; the aluminum map is brighter; Figure 6(b) shows Nd and Al oxides as both elements available in the corroded part; map images are brighter.

Thanh Hung Nguyen et al. [44] presented some new results using low-frequency vibrations for the forging process improvement with different waveforms. Although load reduction is observed, it is critical to compare results found in the literature. Also, the forging process assisted by a PA was presented by using the EMR in low frequency. Both electrical and mechanical component investigations of energy loss are needed to estimate energy reduction [15]. Lee et al. studied the MAO process which was used to create

an oxide film on ZK60 magnesium alloy; effect on corrosion resistance was determined. The impact of electrical parameters such as power mode and applied voltage is calculated. Characterization of the MAO-coated ZK60 Mg alloy and the bare ZK60 Mg alloy is shown in Table 4. The properties of the electrical source and properties of the coating are related [45].

Liu et al. reported that with AlGaIn/GaN, the ohmic contact is obtained. This method is advantageous for fabricating GaN high electron mobility transistor HEMT and advantageous in integrating GaN devices with Si CMOS [46]. Lu et al. investigated the modeling complex forging process; a novel LS-SVM was developed. The entire working region can be divided into many local regions with prior knowledge of HPM. Figure 7 shows the novel LS-SVM modeling method. Local LS-SVM models can accurately show local dynamics. On a local and global scale, regularization is essential. Avoid overfitting each local LSSVM; consider the interaction between neighboring local regions [47].

Luo et al. reported that the corrosion and electrochemical actions of 304L SS at various levels of cold deformation were investigated using potentiodynamic polarization curves, EIS, EBSD, and XPS. With the increase in cold deformation, 304L stainless steel passive current density increases [48]. Yuji Gotoh et al. [49] prepared a specimen in large size; with maximum tensile strength and low permeability, conductivity of

TABLE 4: Characterization of the MAO-coated ZK60 Mg alloy and the bare ZK60 Mg alloy [45].

Sample	Roughness average (μm)	Mean pore diameter (μm)	Area percent of pores (% of total)	The thickness of the coating (μm)
Substrate	0.089	—	—	—
Dc				
250 V	0.190	0.82	5.54	4.8
Unipolar pulsed				
250 V	0.570	2.03	47.8	5.5
300 V	1.439	4.15	36.9	9.8
350 V	2.456	11.2	18.6	19.6
400 V	3.441	13.4	14.2	22.1
Bipolar pulsed				
250 V-20 V	0.193	0.48	28.5	5.5
300 V-20 V	1.950	3.73	18.3	13.2
350 V-20 V	2.844	11.5	9.77	23.5
400 V-20 V	3.017	7.42	5.94	24.3

the steel nanomaterial becomes large. An inspection method was proposed using alternating electromagnetic fields [18]. The results show that as lift-off and tensile strength increase, the flux density amplitude in the search coil decreases [50]. By the proposed inspection method, tensile strength inspection is possible in steel without influencing the lift-off [51]. The tensile strength becomes equal to 1 in a search coil exciting current and flux density B waveform shown in Figure 8.

Poh et al. investigated hybrid magnetic overcoat (Hy-MOC) magnetic properties and inhibition properties. Two types of Hy-MOC were investigated using various types of Co-based alloys. Reactive sputtering with N_2 Hy-MOC(α) used CoCrPt:SiO_2 while Hy-MOC(β) used CoCr_{22} . Figure 9 shows the experimental setup used for the investigation. From the research, it was concluded that Hy-MOC(β) hard disk media has weaker magnetic properties than the Hy-MOC(α), but Hy-MOC(β) is more corrosive resistant. The magnetic media can be protected by a new Hy-MOC system and also provides thermal stability [52].

Zhang et al. examined the influence of microstructure on corrosion behaviour by the laboratory rolling Ni-Fe-Cr alloy 028 which was subject to cold deformation in various degrees. This study involves improvement in various structures via cold rolling. After rolling in the corrosive environment, a significant improvement in corrosion is reported. ND/(111) orientation is reduced as cold reduction increases, resulting in texture described by ND/(110) orientation [53]. Despite the same misorientation between grains, the misorientation distribution inside differently oriented grains was different, as determined by EBSD analysis [54]. Zinno et al. presented an equal little standard subset calculation for the age of differential synthetic aperture radar interferometry distortion guides, and time arrangement appeared. The calculation was ported to the cloud. According to the findings, the P-SBAS cloud migration can process ENVISAT SAR image time series in a short amount of time and at a low cost. The performance of the P-SBAS is compared with the high-performance computing cluster, and the proposed

cloud solution produces no overheat [55]. Kwon et al. arbitrary message signal was utilized to examine the impact of high-pressure deuterium and hydrogen strengthening on the commotion attributes of source adherent square (SF), SF, and line selector (SEL) semiconductors in CMOS picture sensor (CIS) dynamic pixel sensor (RTS). High-pressure D_2 annealing shows the great reduction in $\Delta I_D/I_D$ of SF block. After high-pressure deuterium and hydrogen annealing, $\Delta I_D/I_D$ for SF and SEL has reduced by 48%-52% compared with FG annealing [56]. Xi et al. frequency domain spectroscopy is commonly used for detecting and assessing the oil-paper insulation state, and it has many advantages. Insulation paper/pressboard is considered a direct reflection of mechanical output regarding the degree of polymerization and tensile strength. Table 5 shows the DP and TS values at different stages. Results show that with a decrease of DP and TS, the $\tan \delta$ value varies in exponential form. The established mathematical relation under 0.001 Hz frequency fits best [57].

Yuan et al. reported that the effect of microstructure on aluminum sheet corrosion and mechanism was investigated. The homogenization annealing treatment causes copper segregation on the resolidified clad nanomaterial surface and improved Si diffusion depth during brazing. The fluidity of the brazing layer is stronger without homogenization. After brazing the affected area, Si concentration increases. During brazing in the diffusion zone, dense precipitates were formed, which improves the brazing sheet's corrosion resistance [20]. Li et al. present the feasible test for aluminum alloy bridge deck based on the experimental study on wearability and corrosion resistance. The wearability of the aluminum alloy bridge deck was calculated by a line friction test of standard specimens. To measure the corrosion rate and morphology characteristics of the specimen, electrochemical test was conducted. In nanomaterial science, a field wearability test is commonly used to obtain an accurate measurement. The corrosion resistance test was performed in an acid solution with a pH value of 4.0 to 6.0. Taking

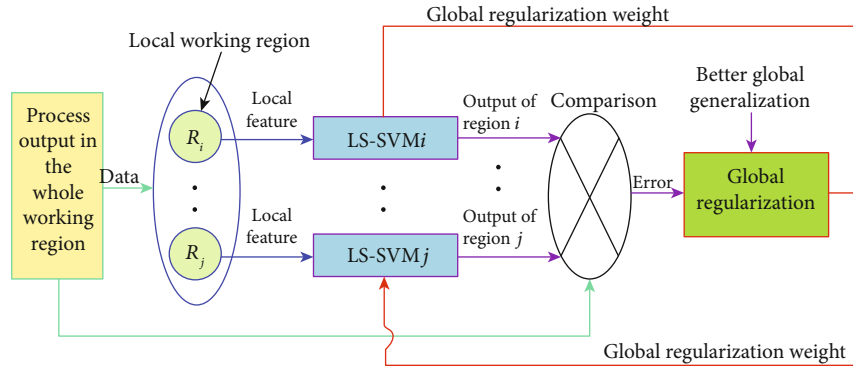


FIGURE 7: Novel LS-SVM method modeling [47].

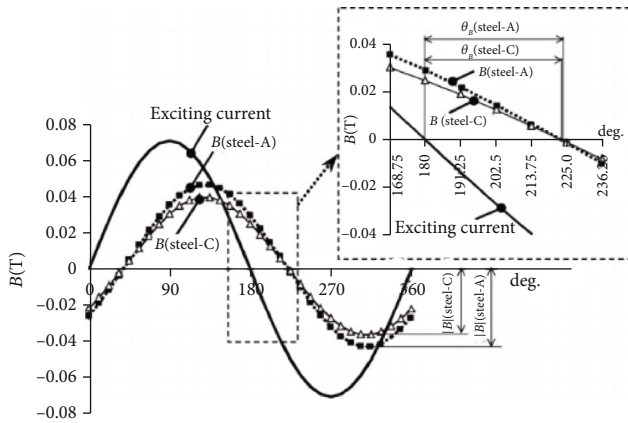


FIGURE 8: Waveforms of the exciting current and flux density in a search coil (calculated, 10 kHz, 100 AT, steel-A and -C, mm) [18].

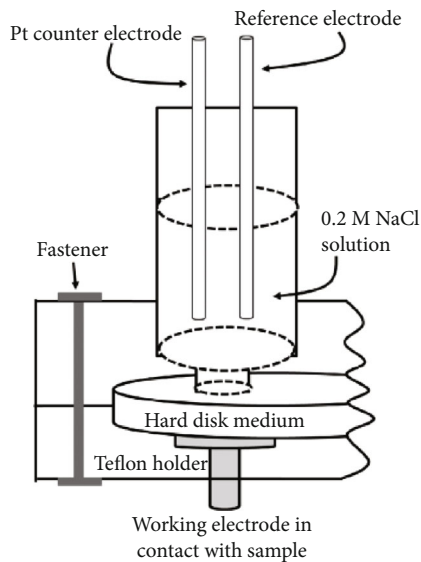


FIGURE 9: Schematic diagram of electrochemical setup used for the investigation [52].

maximum corrosion rate is $34 \mu\text{m/a}$; it takes 30 years to corrode [58]. Seo et al. presented trends of science and engineering expertise in global industries. As the film progresses

through the forging ahead phase, this study shows an increase in science and engineering activities. At last, this paper focuses on exploring the evolutionary patterns of late-comer firm. First, there is an aggregation issue in this report, which ignores the consideration of internal mechanisms and the contributions of universities and public research institutes. Further research that includes internal and external universities' motivations and roles are being investigated and public research institutes and examine the knowledge flow of inventions [59].

Barbi and Judd analyzed stainless steel austenitic intergranular by using transmission electron microscopy of the corroded thin film. To attack in the copper sulphate-sulphuric acid solution, the carbide particles are not susceptible but are subjected to assault in potassium dichromate-nitric acid solution. Exposing the sensitized nanomaterial in a potassium dichromate nitric oxide solution, carbide disappears from corroded grain boundaries. In a commercial annealed nanomaterial for nickel and chromium chemical composition, inhomogeneities were measured [60]. Yeganeh et al. investigate the nanostructured copper stores made with EB-PVD, just as a heartbeat plating procedure is proposed. Transmission electron microscopy was utilized to analyze the morphology of the stored film, and a DEKTAK profilometer was used to assess the roughness of the surface deposits. EB-PVD and pulse plating can be used to create the nanostructured nanomaterial. In this examination, the normal grain size of EB-PVD and heartbeat plated copper was 40 nm. Passivation behaviour was not shown in pulse-plated copper (Figure 10). However, pulse-plated copper in grain size is equal to EB-PVD copper [61].

Arutunow and Darowicki reported that the unique electrochemical impedance spectroscopy (DEIS) method was utilized to recognize rapid impedance changes versus reactivation potential for the AISI 304 hardened steel disintegration measure. During the dissolution of AISI 304 stainless steel, the DEIS technique can detect complex changes in impedance [62]. Arutunow and Darowicki research results into the dissolution of AISI 304 SS in the presence of IGC are presented. According to the experiments, variations in impedance observed during the IGC of AISI 304 SS at various reactivation possibilities were brought about by direct changes in the overall viable surface locale [63]. Iwai et al. made two-course curls out of a pile of four single hotcakes

TABLE 5: DP and TS values at various stages [57].

Day	Degree of polymerization (DP)	Tensile strength (TS)
0	906.9	96.1
10	675.0	79.9
20	508.1	58.1
30	424.9	39.0
35	359.0	34.9
40	286.1	24.0

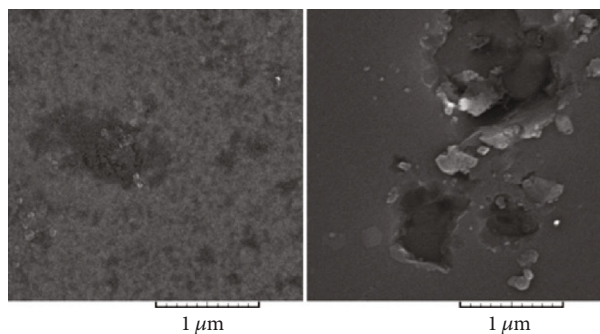


FIGURE 10: Surface morphology after potentiodynamic polarization tests in 0.5 M NaCl solution: (a) EB-PVD copper and (b) pulsed-plated copper [61].

twisted with two various types of created REBCO tapes, with one of the REBCO loops in the hardened steel case cooled by implication through a warm obstruction layer. After the cryocooler stopped cooling, the temperature rose [64]. The test results were very close to the calculated values, showing that controlling the heat flow into the coil is very effective [65].

S. Xu et al. [66] fabricated a TGP with dimensions of 10 cm * 5 cm * 0.28 mm and tested it at various condenser temperatures. At an applied power of 7.9 W, the thermal resistance is estimated to be as low as 4.38 K/W, resulting in a good thermal conductivity of 1398 W/m-K. As the applied power was less than 6.0 W after 45 days, the reliability of TGP output degradation was negligible. At 7.0 W, the thermal resistance increased to 18% [67]. Due to improved evaporation heat transfer, thermal resistance is reduced by increasing the applied power shown in Figure 11(a). Due to partial dry-out condition, a jump in the evaporator temperature as the applied power increase is shown in Figure 11(b).

T. Li et al. [68] investigate the effects of prestrain; a specimen comprised of four types of polyethylene-terephthalate (PET)/Al-doped zinc oxide (AZO) was prepared. The start of pop-in activity is known as the inflexion point. The prestrain added to the PET substrate has an inverse relationship with the pop-in. The sheet resistance is shown to be inversely proportional to the carrier mobility. The magnitude of these defect parameters is inversely proportional to the electrical current calculated at the end of the loading step [69]. Balbola et al. reported that both tensile and compressive uniaxial transverse strains were generated locally using

a new technique. This improvement in affectability of n-type-based 3-D sensors for pressure and out-of-plane typical pressure hits 82% for compressive strain and 21% for pressure. Besides, compressive crossover strains build the pressing factor coefficient of intensely doped n-type silicon up to 80% [70]. Zhang et al. investigated that architecture's two thickest component layers calculated the mechanical behaviour of a REBCO-coated conductor wire under uniaxial stress. The elastic modulus (E) yield stress ($\sigma_{0.2}$), critical stress (σ_c , 0.95), and irreversible stress (σ_{irr} , 0.99) of REBCO wires decreased with increasing copper thickness or copper thickness ratio Cu/(Cu+Sub), according to the experimental results. Critical strain (ϵ_c , 95) and irreversible strain (ϵ_{irr} , 0.99) were unaffected by copper thickness, with intrinsic values of 0.45 and 0.75%. The calculated results are consistent with the measured stress-strain curves, which can be well adapted using the Ramberg-Osgood equation and substrate [71].

Janecska et al. show that enraptured pressure imaging can distinguish lithography surrenders in the 70 nm FinFET gadget's development cycle stream. Running pressure investigation as a screening technique could help engraving and statement measure increase by eliminating probably the main imperfection sources in an extremely short circle on the sweeping wafers without the requirement for costly patterning. Stress imaging can identify process deviations that lead to high defect rates [72]. Daniel and Hubert have proposed ways to apply several equivalent stresses in the case of uniaxial and biaxial mechanical loading, and it has been verified experimentally. The effect of multiaxial stress on multiaxial activity has been contrasted using several numbers of stress-related criteria. The inability of these models to explain the effect of bicompression stress on magnetic activity is their key flaw [73]. Yang researched the impacts of mechanical pressure incited by the door line end (GLE) on gadget attributes for high-k/metal entryway FinFETs utilizing analyses and TCAD recreations. The framework with GLE=100 nm displays 6.3% and 5.7% drive current upgrade over the gadget with GLE=35 nm, separately, as far as n-FinFETs and p-FinFETs. In a TCAD reproduction, the normal channel pressure was diminished from 295 MPa to 168 MPa [74]. Yong et al. reported measurement wire bonding phase; piezoresistive sensors have been demonstrated. According to studies, the voltage output responses are comparable, allowing for proper sample alignment regulation. Various captured bond forces and bonding durations affect the resistors. US signals can be filtered using the FET technique. The stress sensors are found to be capable of capturing various impact forces, bond forces, bonding durations, and US strength [75].

Tingting et al. proposed a degradation model for products in a dynamic environment considering stress drift and shock damage. For some practical problems, the stress drift function may be complex or has a similar form as the shock damage function, making it difficult to separate the effect of the stress drift from that of shock damage. Second, only one type of stress is considered, and for many cases, products experience complex environmental conditions (stress and load) in their life cycle. Third, it is assumed that the stress

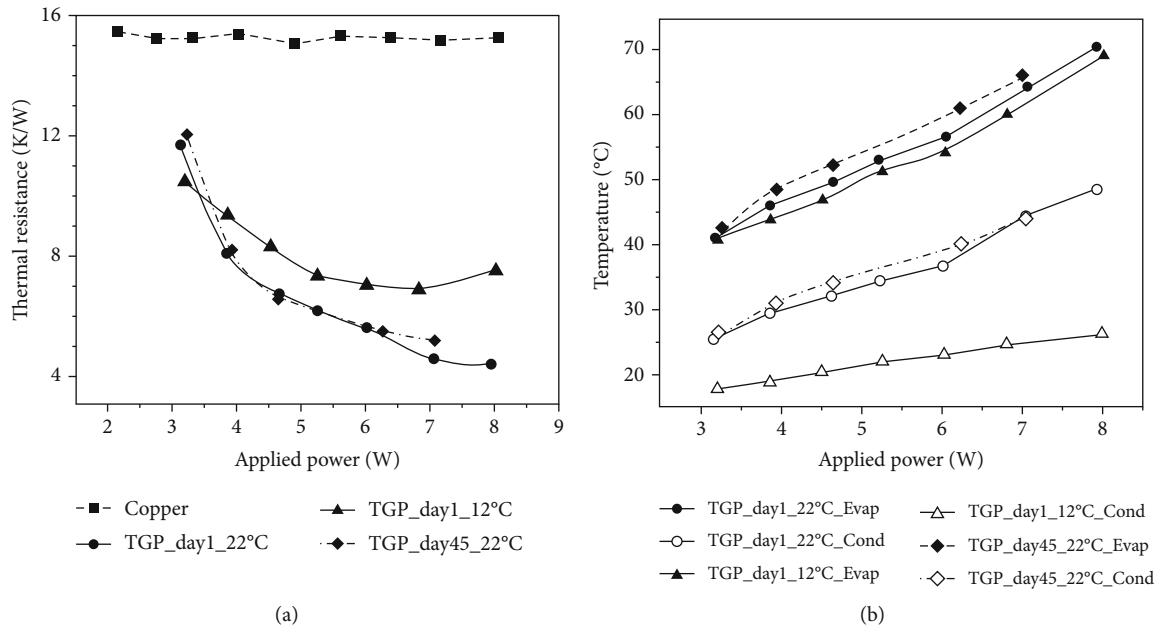


FIGURE 11: (a) Measured thermal resistance of TGP and copper [67]. (b) Measured evaporator and condenser temperature [67].

profile is deterministic and prespecified. The assumption can be relaxed in future research to consider a more complex case that the stress level changes randomly and the stress profile is unknown in advance. A simulation analysis is presented to illustrate the model's implementation, and a case study of miniature light bulbs is used to validate the proposed model's effectiveness [76]. Miyagi et al. utilizing finite element analysis examined the transient temperature appropriation and transient warm pressure circulation inside a covered conductor's loop while cooling with LN₂ (FEA). The effect of the bobbin's actual property estimations on the temperature dissemination and transient warm pressure inside the curl was additionally exhibited. Furthermore, when bobbin nanomaterial with lower thermal conductivity is used, adequate precooling is needed to reduce transient thermal stress [77].

2. Conclusion

Austenitic stainless steel 316 finds extensive use as a structural nanomaterial for nuclear core components because of its good combination of strength, toughness, and resistance to uniform corrosion. Austenitic stainless steel 316 has FCC crystal structure and three major alloying elements—Fe, Cr, and Ni, with its composition as carbon 0.08%, silicon 1%, manganese 2%, chromium 16-18%, nickel 10-14%, and molybdenum 2-3%. Carbon was used as low as commercially feasible to obtain Cr 16-26% and Ni >8%. For austenitic steel, during sensitization, depletion of chromium in the grain boundary occurs. This results in susceptibility to intergranular corrosion. A higher sensitization rate means poor hot strength and mechanical properties at a higher temperature.

It was found that the effect of prestraining of nanomaterials on sensitization phenomena had a comparison. The different sensitization rates were calculated between samples with different degrees (percentage) and deformation modes (hot and cold). The comparative study gave us the best deformation mode and optimized percentage of deformation of the nanomaterial. It serves as a preprocessing mechanical method to decrease the corrosion reactivity and enhance its hot working properties. The metal forming of workpieces was done, and the percentage compression was taken care of like 3%, 6%, and 9%. For corrosion test, Huey test has been used according to ASTM A262 practice C. The corrosion rate is determined from the weight loss after boiling cycles. The analysis of microstructure is done. Microstructure provides a qualitative analysis of sensitization rate while the Huey test provides a quantitative study. The degree of deformation increases as intergranular corrosion decreases.

From the microstructure, it is shown that intergranular corrosion is less in the case of hot forming. Weight loss is more in cold pressing as compared to hot pressing. Hot forming serves as a better preprocessing measure if one needs high hot strength in the nanomaterial. As the deformation increases from more than 9%, the corrosion is very low. Hence, hot forming and a high degree of deformation are good measures to increase hot strength and reduce intergranular corrosion.

Data Availability

The data used to support the findings of this study are included in the article. Should further data or information be required, these are available from the corresponding author upon request.

Disclosure

This study was performed as a part of the Employment of Bahir Dar Institute of Technology, Bahir Dar University, Ethiopia.

Conflicts of Interest

The authors declare that there are no conflicts of interest regarding the publication of this paper.

Acknowledgments

The authors appreciate the supports from Bahir Dar Institute of Technology, Bahir Dar University, Ethiopia. The authors thank Vellore Institute of Technology, Chennai, and Saveetha School of Engineering Chennai for the technical assistance to carry this review work.

References

- [1] H. Wang, L. Chen, B. Dovggy et al., "Micro-cracking, micro-structure and mechanical properties of Hastelloy-X alloy printed by laser powder bed fusion: as-built, annealed and hot-isostatic pressed," *Additive Manufacturing*, vol. 39, p. 101853, 2021.
- [2] H. Tian, Z. Guo, J. Pan et al., "Comprehensive review on metallurgical recycling and cleaning of copper slag," *Resources, Conservation and Recycling*, vol. 168, p. 105366, 2021.
- [3] M. K. Trivedi and R. M. Tallapragada, "A transcendental to changing metal powder characteristics," *Metal Powder Report*, vol. 63, no. 9, pp. 22–29, 2008.
- [4] Q. Yin, Z. Liu, and B. Wang, "Machinability improvement of Inconel 718 through mechanochemical and heat transfer effects of coated surface-active thermal conductive mediums," *Journal of Alloys and Compounds*, vol. 876, p. 160186, 2021.
- [5] P. Snopiński, M. Krol, T. Tański, and B. Krupińska, "Effect of cooling rate on microstructural development in alloy ALMG9," *Journal of Thermal Analysis and Calorimetry*, vol. 133, no. 1, pp. 379–390, 2018.
- [6] V. Paranthaman, K. S. Sundaram, and L. Natrayan, "Influence of SiC particles on mechanical and microstructural properties of modified interlock friction stir weld lap joint for automotive grade aluminium alloy," *SILICON*, vol. 1, pp. 1–11, 2021.
- [7] J. Wu, N. T. Aboulkhair, M. Degano, I. Ashcroft, and R. J. M. Hague, "Process-structure-property relationships in laser powder bed fusion of permanent magnetic Nd-Fe-B," *Materials & Design*, vol. 209, p. 109992, 2021.
- [8] F. Feng, Y. Lian, X. Liu, J. Wang, and Y. Xu, "Effect of high-energy-rate forging on microstructure and properties of W-TaC alloys," *IEEE Transactions on Plasma Science*, vol. 46, no. 6, pp. 2314–2317, 2018.
- [9] R. Suryanarayanan, V. G. Sridhar, L. Natrayan et al., "Improvement on mechanical properties of submerged friction stir joining of dissimilar tailor welded aluminum blanks," *Advances in Materials Science and Engineering*, vol. 2021, 6 pages, 2021.
- [10] Q. Lin, W. Dong, Z. Wang, and D. Xue, "Research on galling behavior in square cup drawing of high tensile strength steel," in *2010 International Conference on Digital Manufacturing & Automation*, vol. 2, pp. 212–215, Changcha, China, 2010.
- [11] V. Paranthaman, K. Shanmuga Sundaram, and L. Natrayan, "Effect of silica content on mechanical and microstructure behaviour of resistance spot welded advanced automotive TRIP steels," *SILICON*, vol. 3, pp. 1–10, 2021.
- [12] A. Sharma, M. A. Hoffmann, P. Matthes et al., "Magnetic tunnel junctions: laser annealing versus oven annealing," *IEEE Transactions on Magnetics*, vol. 55, no. 1, pp. 1–4, 2019.
- [13] M. Sandeep Kauthsa Sharma, S. Umadevi, Y. Sai Sampath et al., "Mechanical behavior of silica fume concrete filled with steel tubular composite column," *Advances in Materials Science and Engineering*, vol. 2021, Article ID 3632991, 9 pages, 2021.
- [14] S. J. Kim, D. H. Yoon, Y. S. Rim, and H. J. Kim, "Low-temperature solution-processed ZrO₂ gate insulators for thin-film transistors using high-pressure annealing," *Electrochemical and Solid State Letters*, vol. 14, no. 11, article E35, 2011.
- [15] H. Zhao, Z. Zhang, H. Zhang, J. Hu, and J. Li, "Effect of aging time on intergranular corrosion behavior of a newly developed LDX 2404 lean duplex stainless steel," *Journal of Alloys and Compounds*, vol. 672, pp. 147–154, 2016.
- [16] D. Veeman, M. S. Sai, P. Sureshkumar et al., "Additive manufacturing of biopolymers for tissue engineering and regenerative medicine: an overview, potential applications, advancements, and trends," *International Journal of Polymer Science*, vol. 2021, Article ID 4907027, 20 pages, 2021.
- [17] B. Eggleston, S. Varlamov, and M. Green, "Large-area diode laser defect annealing of polycrystalline silicon solar cells," *IEEE Transactions on Electron Devices*, vol. 59, no. 10, pp. 2838–2841, 2012.
- [18] F. He, X. Ma, K. Shen, and C. Wang, "Study on material and energy flow in steel forging production process," *IEEE Access*, vol. 8, pp. 12921–12932, 2020.
- [19] M. Terada, M. Saiki, I. Costa, and A. F. Padilha, "Microstructure and intergranular corrosion of the austenitic stainless steel 1.4970," *Journal of Nuclear Materials*, vol. 358, no. 1, pp. 40–46, 2006.
- [20] Z. Yuan, F. Tao, J. Wen, and Y. Tu, "The dependence of microstructural evolution and corrosion resistance of a sandwich multi-layers brazing sheets on the homogenization annealing," *IEEE Access*, vol. 7, pp. 121388–121394, 2019.
- [21] L. Kosec, Š. Šavli, S. Kožuh et al., "Transformation of austenite during isothermal annealing at 600–900 °C for heat-resistant stainless steel," *Journal of Alloys and Compounds*, vol. 567, pp. 59–64, 2013.
- [22] M. V. Klimova, D. G. Shaysultanov, S. V. Zhrebtsov, and N. D. Stepanov, "Effect of second phase particles on mechanical properties and grain growth in a CoCrFeMnNi high entropy alloy," *Materials Science and Engineering: A*, vol. 748, pp. 228–235, 2019.
- [23] H. Sahlaoui, H. Sidhom, and J. Philibert, "Prediction of chromium depleted-zone evolution during aging of Ni-Cr-Fe alloys," *Acta Materialia*, vol. 50, no. 6, pp. 1383–1392, 2002.
- [24] J. Lv, T. Liang, C. Wang, and T. Guo, "Influence of sensitization on passive films in AISI 2205 duplex stainless steel," *Journal of Alloys and Compounds*, vol. 658, pp. 657–662, 2016.
- [25] L. Natrayan, P. S. S. Sundaram, and J. Elumalai, "Analyzing the uterine physiological with mmg signals using svm," *International Journal of Pharmaceutical Research*, vol. 11, no. 2, pp. 165–170, 2019.
- [26] Z. Zhang, H. Zhao, H. Zhang et al., "Effect of isothermal aging on the pitting corrosion resistance of UNS S82441 duplex

- stainless steel based on electrochemical detection," *Corrosion Science*, vol. 93, pp. 120–125, 2015.
- [27] W. Zhang and G. S. Frankel, "Transitions between pitting and intergranular corrosion in AA2024," *Electrochimica Acta*, vol. 48, no. 9, pp. 1193–1210, 2003.
- [28] D. D. Gorhe, K. S. Raja, S. A. Namjoshi, V. Radmilovic, A. Tolly, and D. A. Jones, "Electrochemical methods to detect susceptibility of Ni-Cr-Mo-W alloy 22 to intergranular corrosion," *Metallurgical and Materials Transactions A, Physical Metallurgy and Materials Science*, vol. 36, no. 5, pp. 1153–1167, 2005.
- [29] K. Takahashi, H. Fujishiro, T. Naito, Y. Yanagi, Y. Itoh, and T. Nakamura, "Numerical simulation of electromagnetic and thermal stress in REBaCuO superconducting ring and disk bulks reinforced by stainless steel ring with various widths during field-cooled magnetization," *IEEE Transactions on Applied Superconductivity*, vol. 28, no. 3, pp. 1–5, 2018.
- [30] C. S. S. Anupama, L. Natrayan, E. Laxmi Lydia et al., "Deep learning with backtracking search optimization based skin lesion diagnosis model," *Computers, Materials & Continua*, vol. 70, no. 1, pp. 1297–1313, 2022.
- [31] L. D. Negro, J. H. Yi, M. Hiltunen et al., "Light-emitting silicon-rich nitride systems and photonic structures," *Journal of Experimental Nanoscience*, vol. 1, no. 1, pp. 29–50, 2006.
- [32] M. Forcales, M. Wojdak, M. A. J. Klik et al., "Si nanocrystals as sensitizers for Er PL in SiO₂," *MRS Online Proceedings Library*, vol. 770, pp. 119–123, 2003.
- [33] Hui Chen, Jingsheng Miao, Jun Yan, Zhicai He, and Hongbin Wu, "Improving organic solar cells efficiency through a two-step method consisting of solvent vapor annealing and thermal annealing," *IEEE Journal of Selected Topics in Quantum Electronics*, vol. 22, no. 1, pp. 66–72, 2016.
- [34] Y. Ma, H. Bai, B. Yang, Q. Yu, and Q. Zhang, "Surface modification of carbon steel with plasma chemical vapor deposition for enhancing corrosion resistance in CO₂/brine," *IEEE Transactions on Plasma Science*, vol. 47, no. 5, pp. 2652–2659, 2019.
- [35] A. Bahrami and P. Taheri, "A study on the failure of AISI 304 stainless steel Tubes in a Gas Heater Unit," *Metals (Basel)*, vol. 9, no. 9, p. 969, 2019.
- [36] C. H. Chen, Y. C. Lin, Y. T. Shih et al., "Evaluation of corrosion resistance of ag-alloy bonding wires for electronic packaging," *IEEE Transactions on Components, Packaging and Manufacturing Technology*, vol. 8, no. 1, pp. 146–153, 2018.
- [37] X. Lu, C. Liu, and M. Huang, "Online probabilistic extreme learning machine for distribution modeling of complex batch forging processes," *IEEE Transactions on Industrial Informatics*, vol. 11, no. 6, pp. 1277–1286, 2015.
- [38] S. Yogeshwaran, L. Natrayan, G. Udhayakumar, G. Godwin, and L. Yuvaraj, "Effect of waste tyre particles reinforcement on mechanical properties of jute and abaca fiber - epoxy hybrid composites with pre-treatment," *Materials Today: Proceedings*, vol. 37, no. 2, pp. 1377–1380, 2020.
- [39] A. Salman, D. Catur, I. Made Septayana, and M. Dani Masterawan, "Tensile strength and bending analysis in producing composites by using vacuum resin infusion (VARI) method for high-voltage insulator application," in *2018 2nd International Conference on Applied Electromagnetic Technology (AEMT)*, pp. 39–43, Lombok, Indonesia, 2018.
- [40] S. X. Li, Y. N. He, S. R. Yu, and P. Y. Zhang, "Evaluation of the effect of grain size on chromium carbide precipitation and intergranular corrosion of 316L stainless steel," *Corrosion Science*, vol. 66, pp. 211–216, 2013.
- [41] A. Y. Adesina, Z. M. Gasem, and A. S. Mohammed, "Comparative investigation and characterization of the scratch and wear resistance behavior of TiN, CrN, AlTiN and AlCrN cathodic arc PVD coatings," *Arabian Journal for Science and Engineering*, vol. 44, no. 12, pp. 10355–10371, 2019.
- [42] F. Alhindawi and S. Altarazi, "Predicting the tensile strength of extrusion-blown high density polyethylene film using machine learning algorithms," in *2018 IEEE International Conference on Industrial Engineering and Engineering Management (IEEM)*, pp. 715–719, Bangkok, Thailand, 2019.
- [43] H. Parmar, T. Xiao, Z. Yaoying et al., "Improved corrosion resistance of Co,Al-alloyed NdFeB magnetic nanostructures processed by microwave synthesis techniques," *IEEE Transactions on Magnetics*, vol. 54, no. 11, pp. 1–5, 2018.
- [44] T. H. Nguyen, C. Giraud-Audine, B. Lemaire-Semail, G. Abba, and R. Bigot, "Modeling of forging processes assisted by piezoelectric actuators: principles and experimental validation," *IEEE Transactions on Industry Applications*, vol. 50, no. 1, pp. 244–252, 2014.
- [45] J. L. Lee, S. Y. Jian, K. N. Kuo, J. L. You, and Y. T. Lai, "Effect of surface properties on corrosion resistance of ZK60 mg alloy microarc oxidation coating," *IEEE Transactions on Plasma Science*, vol. 47, no. 2, pp. 1172–1180, 2019.
- [46] Z. Liu, D. Chen, L. Wan, and G. Li, "Micron-scale annealing for ohmic contact formation applied in GaN HEMT gate-first technology," *IEEE Electron Device Letters*, vol. 39, no. 12, pp. 1896–1899, 2018.
- [47] X. Lu, B. Fan, and M. Huang, "A novel LS-SVM modeling method for a hydraulic press forging process with multiple localized solutions," *IEEE Transactions on Industrial Informatics*, vol. 11, no. 3, pp. 663–670, 2015.
- [48] H. Luo, H. Su, G. Ying, C. Dong, and X. Li, "Applied surface science effect of cold deformation on the electrochemical behaviour of 304L stainless steel in contaminated sulfuric acid environment," *Applied Surface Science*, vol. 425, pp. 628–638, 2017.
- [49] Y. Gotoh and N. Takahashi, "Proposal of detecting method of plural cracks and their depth by alternating flux leakage testing: 3-D nonlinear eddy current analysis and experiment," *IEEE transactions on magnetics*, vol. 40, no. 2, pp. 655–658, 2004.
- [50] N. K. Banjara and K. Ramanjaneyulu, "Investigations on behaviour of flexural deficient and CFRP strengthened reinforced concrete beams under static and fatigue loading," *Construction and Building Materials*, vol. 201, pp. 746–762, 2019.
- [51] S. Yogeshwaran, L. Natrayan, S. Rajaraman, S. Parthasarathi, and S. Nestro, "Experimental investigation on mechanical properties of epoxy/graphene/fish scale and fermented spinach hybrid bio composite by hand lay-up technique," *Materials Today: Proceedings*, vol. 37, no. 2, pp. 1578–1583, 2020.
- [52] W. C. Poh, S. N. Piramanayagam, and T. Liew, "Magnetic properties and corrosion resistance studies on hybrid magnetic overcoats for perpendicular recording media," *IEEE Transactions on Magnetics*, vol. 46, no. 4, pp. 1069–1076, 2010.
- [53] L. Zhang, J. A. Szpunar, R. Basu, J. Dong, and M. Zhang, "Influence of cold deformation on the corrosion behavior of Ni-Fe-Cr alloy 028," *Journal of Alloys and Compounds*, vol. 616, pp. 235–242, 2014.
- [54] H. A. Deore, J. Mishra, A. G. Rao, H. Mehtani, and V. D. Hiwarkar, "Effect of filler material and post process ageing

- treatment on microstructure, mechanical properties and wear behaviour of friction stir processed AA 7075 surface composites,” *Surface and Coatings Technology*, vol. 374, pp. 52–64, 2019.
- [55] I. Zinno, S. Elefante, L. Mossucca et al., “A first assessment of the P-SBAS DInSAR algorithm performances within a cloud computing environment,” *IEEE Journal of Selected Topics in Applied Earth Observations and Remote Sensing*, vol. 8, no. 10, pp. 4675–4686, 2015.
- [56] H. Kwon, I. S. Han, S. K. Kwon et al., “Effects of high-pressure annealing on random telegraph signal noise characteristic of source follower block in CMOS image sensor,” *IEEE Electron Device Letters*, vol. 34, no. 2, pp. 190–192, 2013.
- [57] X. Xi, H. Wang, W. Wang, Y. Xiao, Q. Li, and W. Liu, “The study on the relationship of frequency domain spectroscopy of oil-paper insulation with degree of polymerization and tensile strength,” in *2018 12th International Conference on the Properties and Applications of Dielectric Materials (ICPADM)*, pp. 801–804, Xi'an, China, 2018.
- [58] J. Li, H. Ban, Y. Shi, Y. Wang, and Z. Zhang, “Experimental research on the wearability, corrosion resistance, and life assessment of an aluminum alloy bridge deck,” *Tsinghua Science and Technology*, vol. 15, no. 5, pp. 566–573, 2010.
- [59] E. Y. Seo, J. Y. Choung, and H. R. Hwang, “The changing patterns of knowledge production of catch-up firms during the forging-ahead period: case study of Samsung Electronics Co. (SEC),” *IEEE Transactions on Engineering Management*, vol. 66, no. 4, pp. 621–635, 2019.
- [60] N. C. Barbi and G. Judd, “Microstructure and microsegregation effects in the intergranular corrosion of austenitic stainless steel,” *Metallurgical and Materials Transactions B*, vol. 3, no. 11, pp. 2959–2964, 1972.
- [61] M. Yeganeh, M. Motamedi, and M. Eskandari, “Comparison of corrosion resistance of nanostructured copper produced in vacuum and electrolytic solution in neutral chloride media,” *Micro & Nano Letters*, vol. 6, no. 6, pp. 402–404, 2011.
- [62] A. Arutunow and K. Darowicki, “DEIS assessment of AISI 304 stainless steel dissolution process in conditions of intergranular corrosion,” *Electrochimica Acta*, vol. 53, no. 13, pp. 4387–4395, 2008.
- [63] A. Arutunow and K. Darowicki, “DEIS evaluation of the relative effective surface area of AISI 304 stainless steel dissolution process in conditions of intergranular corrosion,” *Electrochimica Acta*, vol. 54, no. 3, pp. 1034–1041, 2009.
- [64] S. Iwai, H. Miyazaki, Y. Otani et al., “A conduction-cooled REBCO magnet with a single-stage GM cryocooler and a stainless steel case for storing the coil and covering it from thermal radiation,” *IEEE Transactions on Applied Superconductivity*, vol. 27, no. 4, pp. 1–5, 2017.
- [65] A. S. Mitko, D. R. Streltsov, P. V. Dmitryakov, A. A. Nesmelov, A. I. Buzin, and S. N. Chvalun, “Evolution of morphology in the process of growth of island poly(p-xylylene) films obtained by vapor deposition polymerization,” *Polymer Science, Series A*, vol. 61, no. 5, pp. 555–564, 2019.
- [66] S. Xu, Y. Wang, and Y. Tan, “Influence of Discharge Flow of Daily Regulating Hydropower Station on Habitat of Schizothoraxprenanti in Downstream River Channel,” *Water Resources and Power*, vol. 1, p. 7, 2013.
- [67] X. Zeng and H. Jiang, “In Situ Fabrication and Actuation of Polymer Magnetic Microstructures,” *Journal of Microelectromechanical Systems*, vol. 20, no. 4, pp. 785–787, 2011.
- [68] T. Li, B. H. Wu, and J. F. Lin, “Effects of pre-strain applied at a polyethylene terephthalate substrate before the coating of TiO₂ film on the coating film quality and optical performance,” *Thin Solid Films*, vol. 519, no. 22, pp. 7875–7882, 2011.
- [69] T. C. Li, C. F. Han, B. H. Wu, P. T. Hsieh, and J. F. Lin, “Effects of prestrain applied to a polyethylene terephthalate substrate before the coating of Al-doped ZnO film on film quality, electrical properties, and pop-in behavior during nanoindentation,” *Journal of Microelectromechanical Systems*, vol. 21, no. 5, pp. 1059–1070, 2012.
- [70] A. A. Balbola, M. O. Kayed, and W. A. Moussa, “Experimental characterization of the influence of transverse prestrain on the piezoresistive coefficients of heavily doped n-type silicon,” *IEEE Transactions on Electron Devices*, vol. 65, no. 11, pp. 5002–5008, 2018.
- [71] Y. Zhang, D. W. Hazelton, R. Kelley et al., “Stress-strain relationship, critical strain (stress) and irreversible strain (stress) of IBAD-MOCVD-based 2G HTS wires under uniaxial tension,” *IEEE Transactions on Applied Superconductivity*, vol. 26, no. 4, pp. 1–6, 2016.
- [72] M. Janecska, Z. Kovacs, A. Pongracz, and M. Tallian, “Correlation study of bulk Si stress and lithography defects using polarized stress imager,” *IEEE Transactions on Device and Materials Reliability*, vol. 20, no. 1, pp. 221–223, 2020.
- [73] L. Daniel and O. Hubert, “Equivalent stress criteria for the effect of stress on magnetic behavior,” *IEEE Transactions on Magnetics*, vol. 46, no. 8, pp. 3089–3092, 2010.
- [74] P. Y. Yang, “Effect of gate-line-end-induced stress and its impact on device’s characteristics in FinFETs,” *IEEE Electron Device Letters*, vol. 37, no. 7, pp. 910–912, 2016.
- [75] W. Y. Yong, X. Zhang, T. C. Chai, A. Trigg, N. B. Jaafar, and G. Q. Lo, “In situ measurement and stress evaluation for wire bonding using embedded piezoresistive stress sensors,” *IEEE Transactions on Components, Packaging and Manufacturing Technology*, vol. 3, no. 2, pp. 328–335, 2013.
- [76] H. Tingting, P. Bo, Z. Yuepu, and Y. Zixuan, “Reliability assessment considering stress drift and shock damage caused by stress transition shocks in a dynamic environment,” *Journal of Systems Engineering and Electronics*, vol. 30, no. 5, pp. 1025–1034, 2019.
- [77] D. Miyagi, M. Kato, Y. Yoshida, and M. Tsuda, “Influence of a coil bobbin on transient thermal stress in a REBCO pancake coil,” *IEEE Transactions on Applied Superconductivity*, vol. 28, no. 4, pp. 1–5, 2018.